Materials & Design 259 (2025) 114882

Contents lists available at ScienceDirect

Materials & Design

journal homepage: www.elsevier.com/locate/matdes

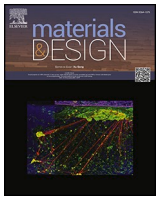

Microstructural evolution, deformation modes, and failure mechanisms in laser powder bed fusion processed nickel-free and 316L stainless steels☆

Siddharth Suman [a,1], Sneha Goel [a,1], Juhani Rantala [a], Asta Nurmela [a], Abhinav Anand [b,2], Ashish Ganvir [b], Ran Sui [c], Zaiqing Que [a,*]

[a] VTT Technical Research Centre of Finland, Espoo 02150, Finland
[b] Department of Mechanical and Materials Engineering, University of Turku, Turku 20520, Finland
[c] Department of Energy and Power Engineering, Tsinghua University, Beijing 100084, China

ARTICLE INFO

Keywords:
Laser based powder bed fusion
Additive manufacturing
Nickel-free steel
Stainless steel
Microstructure

ABSTRACT

This study investigates the influence of microstructures on mechanical behavior and failure mechanisms of laser based powder bed fusion processed nickel-free and 316L stainless steels using small punch testing, nano-indentation, and miniaturized tensile testing. The as-printed 316L with a fully austenitic structure and high-density dislocation cells exhibited a nanohardness of 3.0 GPa, tensile strength of 600 MPa, and elongation close to 60 %, with failure occurring through ductile microvoid coalescence. In contrast, the as-printed nickel-free stainless steel with a fully ferritic matrix and random dislocation networks showed a high nanohardness of 4.94 GPa, but poor ductility of 2 % and transgranular cleavage fracture. Heat treatment at 950 °C for 30 min transformed the nickel-free steel into a duplex microstructure (56 % ferrite and 41 % austenite, with a minor 3 % Chi phase), reducing dislocation density and inducing stacking faults. This resulted in moderate improvement in tensile strength as well as ductility and a mixed fracture mode. Post-mortem analysis revealed that Chi phase assisted crack initiation and strain localization was observed near coarse grains. The evolution of low-angle to high-angle grain and twin boundaries promoted plastic deformation. These results highlight the importance of phase engineering and microstructural control in optimizing the ductility and toughness of nickel-free steels.

1. Introduction

Stainless steels are commonly used structural materials because of their excellent corrosion resistance and superior mechanical properties [1,2]. Stainless steels are usually processed via casting or wrought processes. Although these traditional manufacturing processes have their advantages, significant efforts have also been invested in developing advanced manufacturing techniques that offer unprecedented design freedom for complex geometries, reduced cost and lead time, as well as improved long-term performance in harsh environments. Among the advanced manufacturing technologies developed in recent decades, additive manufacturing (AM), also commonly known as 3D printing, has emerged as one of the most promising approaches [3–5].

Laser based powder bed fusion (PBF-LB) is among the most widely applied AM techniques for metals [6–11], with extensive adoption across various industrial sectors [12]. Since 2022, PBF-LB fabricated 316L stainless steel components have been successfully used in nuclear reactor cores [13], demonstrating excellent performance under highly demanding conditions. PBF-LB 316L stainless steels possess elevated mechanical strength in comparison to their wrought counterparts due to its unique hierarchical microstructure formed during the rapid solidification process [14–16]. However, as-printed parts often exhibit microstructural inhomogeneity, suboptimal phase composition, anisotropy, residual stresses, *etc*. which can adversely affect their mechanical performance. For many demanding applications, materials with homogeneous equiaxed microstructure are preferred due to their favorable combination of ductility and strength. Accordingly, post-processing thermal treatments are commonly employed not only to achieve equiaxed grain structures but also to alleviate these inhomogeneities, induce phase transformations, and tailor other microstructural features,

☆ This article is part of a special issue entitled: 'Additive Manufacturing' published in Materials & Design.

* Corresponding author.
E-mail address: zaiqing.que@vtt.fi (Z. Que).
[1] First authors.
[2] Current address: Department of Mechanical Engineering, Politecnico di Milano, Via La Masa 1, 20156 Milano, Italy.

https://doi.org/10.1016/j.matdes.2025.114882
Received 24 July 2025; Received in revised form 4 October 2025; Accepted 5 October 2025
Available online 8 October 2025

thereby optimizing the mechanical properties of PBF-LB printed materials [17–20].

In austenitic stainless steels, such as 316L, nickel stabilizes the austenitic phase, enhancing mechanical properties and corrosion resistance at high temperatures, but it also promotes the formation of radiation-induced defects, increasing susceptibility to embrittlement in irradiation environments [21,22]. Furthermore, the environmental impact of nickel extraction and processing has led to calls for more sustainable alternatives [23]. Nickel mining and refining contribute to significant environmental pollution, making it less desirable for use in industries with growing sustainability goals. Additionally, nickel is known to cause allergic reactions in a significant part of the population [24]. Nickel-free (Ni-free) alloys that use alternative austenite stabilizers such as nitrogen and manganese can enhance mechanical properties, reduce environmental impact, minimize the risk of allergic reactions, and mitigate radiation-induced embrittlement [25–28]. Moreover, AM techniques like PBF-LB allow for tailored microstructures, optimizing these alloys for various application scenarios.

While promising, PBF-LB Ni-free steels have not yet been fully characterized in terms of their detailed mechanical behavior and failure mechanisms [29–31]. Furthermore, the influence of post-processing techniques, particularly heat treatment, on their microstructure and mechanical properties has yet to be thoroughly investigated. Heat treatment can significantly influence phase composition, grain structure, dislocation configuration as well as other intrinsic defect distributions, which in turn affect deformation and failure behaviors. Investigating these effects is essential for evaluating their suitability for different demanding applications.

The present study explores AM alloys with crystal structure beyond the commonly studied face-centered cubic (FCC) structures. Specifically, it examines the relationship between the printing microstructure, and deformation and failure mechanisms in PBF-LB processed Ni-free and 316L stainless steels using small punch testing, nanoindentation, miniaturized tensile testing, and microstructural characterization. The Ni-free stainless steels were examined in the as-printed and heat-treated conditions to assess the effects of thermal processing on their microstructure and consequent mechanical performance.

2. Experimental details

2.1. Materials and specimens

Two types of gas-atomized stainless steel powders were used in this study. The 316L powder with an average particle size of 31.5 μm was sourced from SLM Solutions Group AG, while the Ni-free stainless steel powder with an average particle size of 27.5 μm was obtained from Sandvik Osprey Ltd. The utilized virgin 316L and Ni-free powder was fully ferritic. To stabilize the austenite phase in this Ni-free alloy, higher Mn and N contents were employed compared to conventional AISI 316L stainless steel.

Specimens were printed using an Aconity MIDI + PBF-LB machine (Aconity3D, Germany) equipped with a single mode, continuous wave, infrared fiber laser. A laser spot diameter of 80 μm was used for both 316L and Ni-free stainless steels. All the samples were printed using a stripe-hatching scanning strategy, with 5 mm wide stripes and a 67° rotation of the scanning direction between successive layers. This approach altered the thermal gradient direction between layers, helping to minimize and uniformly distribute residual stress, thereby reducing the likelihood of cracking during printing. During the sample fabrication, argon gas was supplied to the build chamber to maintain an oxygen concentration below 500 ppm and maximize specimen density. The powder morphology and powder size distribution (PSD) can be found in [32].

For the reference material 316L, the optimized process parameters recommended by the machine manufacturer (Aconity3D) were employed, including a laser power of 150 W, scanning speed of 900 mm/s, hatch distance of 0.08 mm, and layer thickness of 0.03 mm. These conditions resulted in samples with a relative density of 99.8 %. The process parameters for Ni-free stainless steel were selected based on an extensive design of experiments aimed at maximizing specimen density [32]. Samples were produced using a laser power of 140 W, scanning speed of 600 mm/s, hatch distance of 0.08 mm, and layer thickness of 0.03 mm, resulting in a relative density 98.83 %, as measured by Archimedes method.

To induce phase transformation, the Ni-free stainless steel samples were subjected to a systematically designed post-printing isothermal heat treatment at 950 °C for 30 min, followed by water quenching. Based on the Thermo-Calc phase diagram predictions [32] and confirmed by experimental observations, this heat treatment procedure results in a phase transformation from a fully ferritic structure in the as-printed condition to a duplex microstructure. It is noteworthy that due to the low ductility of the Ni-free steels, pre-existing sub-micron cracks were locally observed in the as-printed material.

2.2. Mechanical testing

Miniature tensile tests were conducted using an MTS servo hydraulic testing machine in displacement control mode according to ISO-6892 standard at room temperature. The technical drawing of miniaturized tensile test specimens is provided in Fig. 1. The tensile specimens were tested at two different strain rates of $2.5 \times 10^{-4}\ s^{-1}$ and $1.25 \times 10^{-5}\ s^{-1}$ to assess the effects of deformation rate. The yield strength was determined as the 0.2 % offset yield strength and the tensile strength was taken at the maximum force applied during the test.

Small punch tests were conducted according to EN10371 at a constant crosshead displacement rate of 0.3 mm/min. Cylindrical test specimens with P1200 finish, 8 mm diameter, and 0.5 mm ± 0.005 mm thickness were utilized. The specimen deflection was measured from below by a displacement transducer. Three tests were conducted for each material at room temperature to evaluate repeatability.

Nanoindentation and Vickers microhardness tests were performed on mounted specimens with an oxide polishing suspension (OPS) finish. Nanoindentation tests were performed using an Anton Paar Ultra Nanoindentation Tester UNHT with a linear loading method up to a maximum indentation depth of 1 μm. A loading and unloading rate of 7.5 mN/min was applied, with a 10-second pause at maximum load. Ten nanoindentation indents were made at room temperature with a 30 μm spacing between each indent. Vickers microhardness measurements were performed using a Struers DuraScan-80 automatic indenter with a 1 kg load (HV1). Ten microhardness indents were made at room

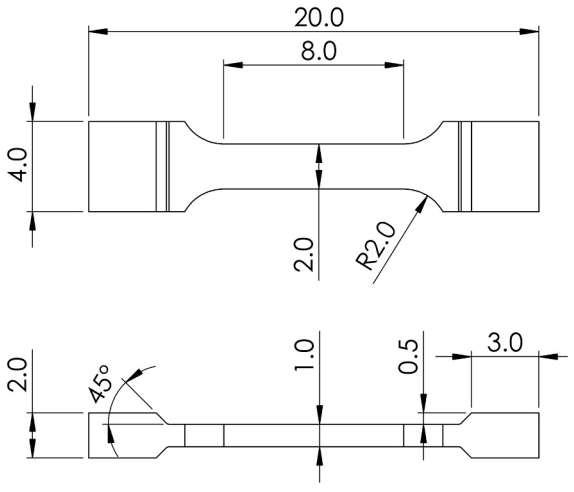

Fig. 1. Technical drawing of miniaturized tensile test specimen. All dimensions are in millimeters.

Table 1
Measured chemical compositions (wt.%) of as-printed PBF-LB Ni-free and 316L stainless steel powders applied and printed specimens.

Material	Fe	Cr	Ni	Mo	Mn	Si	N	O	C	S	P
Ni-free powder	Bal.	17.3	0.10	3.20	11.4	0.70	0.18	0.16	0.03	0.005	0.017
Ni-free printed sample	Bal.	17.7	0.13	3.17	9.91	0.78	0.15	0.048	0.03	0.004	0.017
316L powder	Bal.	17.84	12.5	2.43	0.73	0.9	0.10	0.02	0.02	0.01	0.007
316L printed sample	Bal.	17.9	12.8	2.33	0.73	0.69	0.08	0.026	0.02	0.004	0.01

temperature with a 1 mm spacing between each indent.

2.3. Elemental and microstructural characterization

Chemical composition analysis of the as-printed Ni-free and 316L stainless steel specimens was performed using Optical emission spectrometry (OES) and carrier gas measurements. The OES measurements were conducted with an ARL8860 device. Nitrogen and oxygen contents were determined according to the carrier gas method "T001-023″ using a LECO TC-500 analyzer. The measured compositions are summarized in Table 1.

Microstructural characterization was performed using a Zeiss Crossbeam 540 scanning electron microscope (SEM) equipped with an EDAX Hikari Plus electron backscatter diffraction (EBSD) detector. Electron channeling contrast imaging (ECCI) was conducted with the solid-state four-quadrant backscatter detector. The parameters for backscattered electrons (BSE) imaging were set at 15 keV and 1.5nA, with a working distance (WD) of 5–7 mm. For EBSD analysis, the WD was set to 11–14 mm, employing a step size of 50–300 nm depending on the scanned area. Inversed pole figures (IPF), phase maps, and kernel average misorientation (KAM) maps were analyzed based on the EBSD data.

3. Results

3.1. Microstructural characterization of as-printed and heat-treated materials

Fig. 2 presents EBSD maps illustrating the microstructures of the 316L as well as as-printed and heat-treated Ni-free stainless steel samples investigated in this study. The as-printed 316L matrix consisted almost entirely of austenite (99.9 %), while the as-printed Ni-free steel was primarily ferritic (99.9 % ferrite). Following heat treatment, the heat-treated Ni-free steel developed a duplex microstructure comprising of nearly 56 % ferrite, 41 % austenite, and 3 % Chi phase. These as well as other microstructural features are presented in detail below.

Both 316L and as-printed Ni-free stainless steel exhibited strong texture and a nearly equal proportion of low-angle grain boundaries (LAGBs, 2°–10°) and high-angle grain boundaries (HAGBs, >10°). The heat-treated Ni-free stainless steel sample is characterized by high-angle boundaries and the local formation of annealing twins within the grains. Table 2 summarizes the portions of HAGBs, LAGBs and the fraction of twins in the HAGBs in these materials. The fraction of HAGBs in the studied materials can be ranked as 316L ≈ as-printed Ni-free steel < heat-treated Ni-free steel. Qualitative analysis of KAM maps (Fig. 2(f) vs. (i)) indicates a reduction in geometrically necessary dislocation (GND) density after heat treatment. Quantitative GND-based dislocation density analysis revealed values of $2.02 \times 10^{14}\ m^{-2}$ for as-printed 316L, $1.71 \times 10^{14}\ m^{-2}$ for as-printed Ni-free stainless steel, and $0.74 \times 10^{14}\ m^{-2}$ for heat-treated Ni-free stainless steel. This reduction is consistent with dislocation recovery during heat treatment.

Moreover, from the EBSD orientation maps with highlighted grain boundaries the heat-treated Ni-free samples were found to exhibit bimodal grain structure, the coarse grains being surrounded by fine ones. These fine grains consisted of austenitic FCC phase formed at the grain boundaries of ferritic body-centered cubic (BCC) grains during the isothermal heat treatment. Additionally, a third phase — the Chi phase — was observed in the heat-treated Ni-free specimens as illustrated by EBSD phase map in Fig. 2(j) and EDS results in Fig. 2(k-o). The Chi phase typically precipitates either at the grain boundaries of FCC grains or the interface between FCC and BCC phases and is enriched in Mo and depleted in Fe compared to the matrix. The ferrite phase has higher concentrations of Mo and Cr and lower concentration of Mn compared to the austenite phase.

Fig. 3 presents ECCI images illustrating the microstructures of the 316L as well as as-printed and heat-treated Ni-free stainless steel samples. Fig. 3(a-b) show the 316L grains with a cellular structure of high-density dislocations tangled at the cell boundaries. The cell size in the sample is measured to be ≈400–600 nm. The as-printed Ni-free stainless steel reveal random dislocation arrangement in the grains. After heat treatment, the dislocation density in the Ni-free stainless steel was significantly reduced, and a large amount of stacking faults formed within the austenitic grains and Chi phase. Furthermore, ECCI analysis of multiple regions in the heat-treated Ni-free steel suggests a stacking fault density of approximately $5.2 \times 10^{13}\ m^{-2}$.

3.2. Nanohardness and microhardness measurements

Fig. 4 presents the load–displacement curves obtained from nanoindentation testing, comprising 10 indentations for each of the three materials. Fig. 5 depicts the summary of the nanohardness and elastic modulus results. The as-printed Ni-free steel exhibited the steepest slopes during both loading and unloading phases, indicating the highest stiffness and hardness among the studied materials. The heat-treated Ni-free steel showed intermediate stiffness and elastic recovery, reflecting the effects of microstructural changes induced by the heat treatment. In contrast, 316L stainless steel displayed the lowest slope and elastic recovery. The elastic modulus values obtained from nanoindentation tests were 177 ± 29 GPa for 316L, 192 ± 20 GPa for the as-printed Ni-free steel, and 190 ± 23 GPa for the heat-treated Ni-free steel. The nanohardness values obtained were 3.0 ± 0.2 GPa for 316L, 4.94 ± 0.25 GPa for the as-printed Ni-free steel, and 3.37 ± 0.24 GPa for the heat-treated Ni-free steel.

Vickers microhardness of 316L, as-printed and heat-treated Ni-free stainless steel samples followed a trend consistent with the nanohardness measurements, with values 229 ± 4 HV1, 359 ± 15 HV1, and 273 ± 7 HV1, respectively. As-printed Ni-free steel exhibited maximum hardness owing to its fully ferritic structure. The ferrite phase (as-printed Ni-free) is harder than the austenite phase (316L). Since the heat-treated Ni-free steel contains both phases, its hardness falls between the as-printed Ni-free steel and 316L.

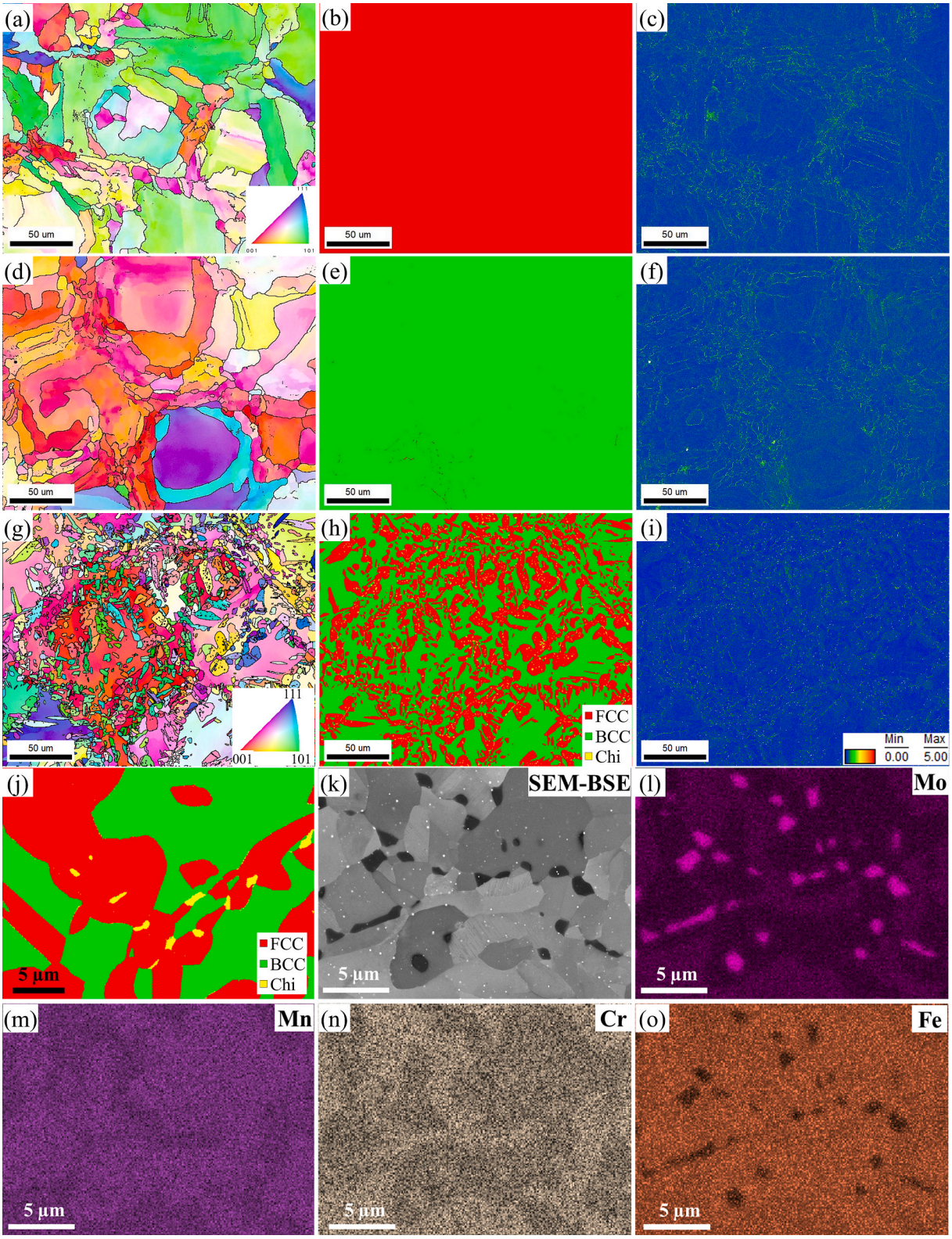

Fig. 2. EBSD orientation distribution, phase, and KAM maps of PBF-LB (a-c) 316L, (d-f) as-printed Ni-free stainless steel and (g-i) heat-treated Ni-free stainless steel sample, respectively. Chi phase precipitates discerned at higher magnification in (j) EBSD phase map, and (k) BSE micrograph and corresponding (l-o) energy-dispersive X-ray spectroscopy (EDS) wt.% maps for the heat treated Ni-free stainless steel.

Table 2
Summary of phase composition and grain boundary characteristics in the studied samples.

Material	Grain size (μm)	Phase	Dislocation/ stacking fault	LAGB (%)	HAGB (%)	Twin boundaries portion in HAGB (%)
316L	35 ± 18	FCC	Cells	48	52	–
As-printed Ni-free	43 ± 21	BCC	Random dislocations	49	51	–
Heat-treated Ni-free	Bimodal	BCC + FCC	Stacking faults	8	92	9

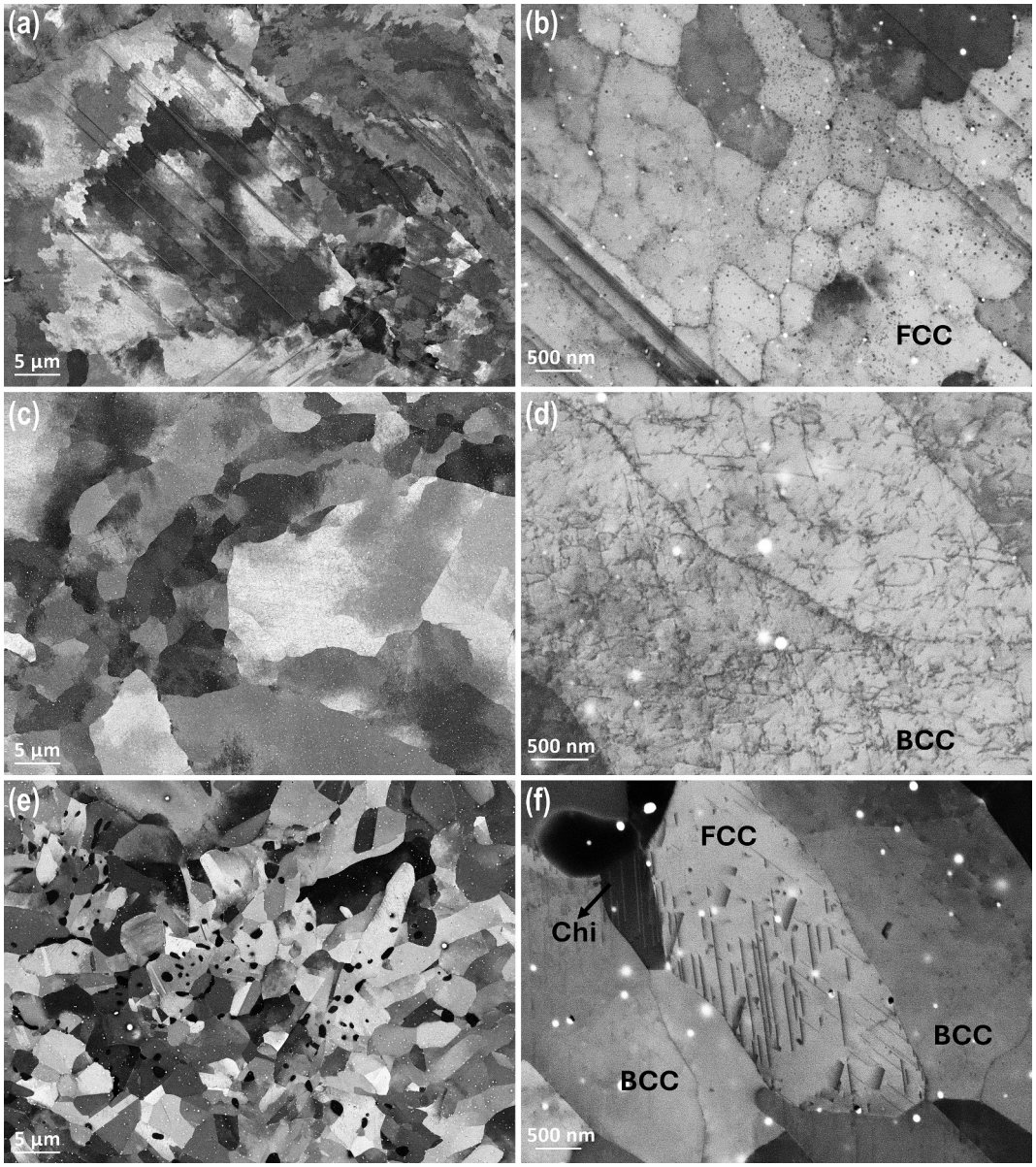

Fig. 3. ECCI images of PBF-LB (a-b) 316L, (c-d) as-printed Ni-free stainless steel and (e-f) heat-treated Ni-free stainless steel samples.

3.3. Small punch testing

Fig. 6 shows the small punch testing results of the investigated materials. Ductile fracture was observed in 316L, whereas the as-printed and heat-treated Ni-free stainless steel samples exhibited varying degrees of brittleness. The as-printed 316L sample exhibited the highest tensile strength, and the greatest ductility. The heat-treated Ni-free sample showed improved ductility over the as-printed Ni-free sample despite a reduction in yield stress.

Fig. 7 presents the SEM images of the fracture surfaces of the small punch tested specimens. 316L specimen failed in a ductile transgranular mode with microvoid coalescence. The as-printed Ni-free stainless steel specimen exhibited a cleavage fracture mode. The fracture surface on heat-treated Ni-free stainless steel specimen revealed a mixed mode of fracture, *i.e.* the fracture initiated with a ductile fracture having dimples and then propagated with transgranular brittle fracture. The initiation with dimples was associated with the precipitates in the material matrix, as shown in Fig. 7(i).

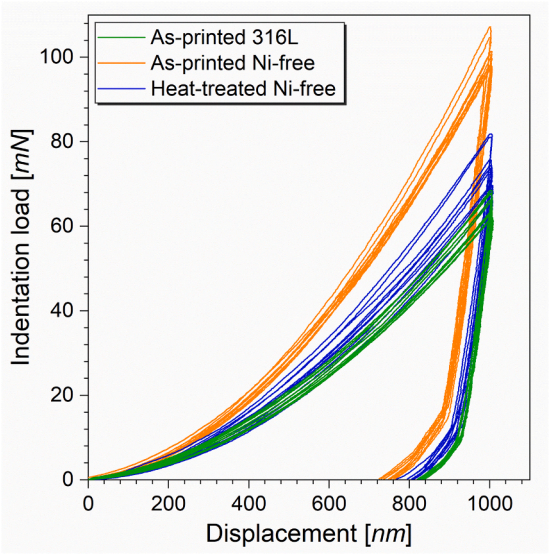

Fig. 4. Summary of nanoindentation results for PBF-LB 316L, as-printed Ni-free stainless steel, and heat-treated Ni-free stainless steel.

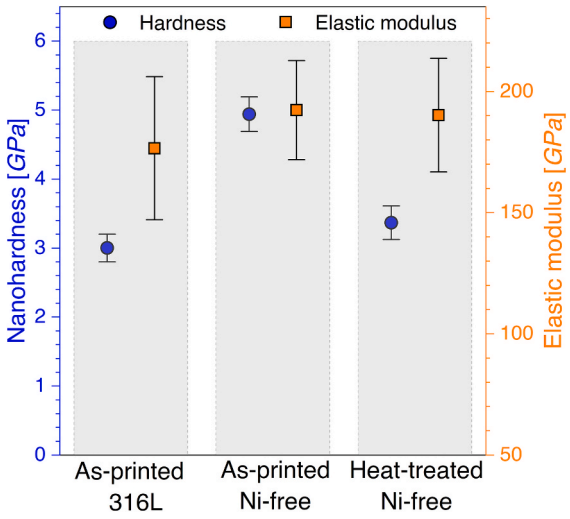

Fig. 5. Summary of nanohardness and elastic modulus results for PBF-LB 316L, as-printed Ni-free stainless steel, and heat-treated Ni-free stainless steel.

3.4. Miniaturized tensile testing

The stress–strain responses of PBF-LB 316L, as-printed Ni-free steel, and heat-treated Ni-free steel samples at the strain rate of $2.5 \times 10^{-4}\ s^{-1}$ as per ISO-6892 standard are presented in Fig. 8. The 316L as-printed sample exhibited highest tensile strength, reaching around 600 MPa, and the greatest ductility of ≈ 60 % at the standard strain rate. The heat-treated Ni-free sample showed improved performance over the as-printed Ni-free sample, achieving a relatively higher tensile strength of about 115 MPa compared to 90 MPa and greater ductility, sustaining 6 % strain versus 2 % strain before failure. This indicates that heat treatment enhances both the strength and ductility of the Ni-free steel, though it still performs far inferior to the 316L as-printed steel.

Fig. 9 shows the comparison of stress strain curves of the materials investigated at two strain rates. Similar tensile performance characteristics are also observed at the lower strain rate. The as-printed 316L and as-printed Ni-free steel exhibited a positive strain rate sensitivity while the heat-treated Ni-free sample showed a negative strain rate sensitivity.

SEM images of the corresponding fracture surfaces of the materials, shown in Fig. 10(a-c), indicate that there is evident necking in 316L material. The 316L stainless steel specimen failed with a ductile mode by microvoid coalescence. The as-printed Ni-free stainless steel specimen exhibited a very flat fracture surface with purely cleavage fracture, refer Fig. 10(d-f). The fracture surface on heat-treated Ni-free stainless steel specimen, as shown in Fig. 10(g-i), reveals a mixed mode of fracture, where ductile tearing ridges with dimples can be observed between the cleavage regions with transgranular brittle fracture.

Cross-sectional BSE images in Fig. 11(a-c) reveal the nanovoid and microvoid formation behind the evident necking and plastic deformation (with extensive contours) under the fracture surface of 316L material. Fig. 11(d-f) indicate transgranular cleavage fracture without apparent deformation on as-printed Ni-free stainless steel specimen. For the heat-treated Ni-free stainless steel samples, Fig. 12 reveals that the cracks propagate primarily along the coarse BCC grains. Furthermore with a closer look, Fig. 13(a-b) and (d-e) illustrate two representative cross-sectional regions beneath the cleavage fracture surface and the ductile fracture surface, where no apparent plastic deformation and extensive deformation were observed, respectively. In both regions, the Chi phase precipitated either at the grain boundaries of FCC grains or the interface between FCC and BCC grains evidently present a significant promoting role for the crack propagation. The voids were formed at the interface between the Chi phase and the matrix.

4. Discussion

4.1. Material processing – microstructure correlation in as-printed and post-treated PBF-LB parts

In the fully austenitic 316L sample, the metastable cellular structures with high-density dislocations were formed as a result of cellular solidification of the melt, driven by the high cooling rate during the rapid scanning process. Such cellular structures are typically observed in Fe-Cr-Ni alloys such as 316L, where the addition of Ni increases the stacking fault energy thereby facilitating dislocation cross-slip [33]. These sub-micron cellular structures are characteristic of AM processed austenitic stainless steels [34]. Additionally, the nano-sized oxides present mainly at the cell boundaries, originate from the oxygen absorbed at the powder surface and the oxygen in the argon gas used to protect the melting pool during printing process [3].

The Ni-free stainless steel samples exhibited fully ferritic microstructure. This can be explained by the chemical composition of the alloy being high in Cr/Ni ratio and the ultra-high cooling rates during PBF-LB processing, as explained in detail previously by the authors [29]. PBF-LB processed 2507 duplex stainless steel yielded a microstructure with approximately 98 % ferrite and only 2 % austenite [35]. Notably, an earlier study by S. David *et al.* [36] involving welding of different grades of steels under extremely high cooling rates—on the order of 10^6 °C/s, comparable to those in PBF-LB—reported the formation of a fully ferritic microstructure, particularly in steels with a high Cr/Ni equivalent ratio. Whereas at lower cooling rates, achieved by slower welding speeds, the as-welded structures were duplex with presence of both austenite and ferrite. In the as-printed Ni-free stainless steel with ferritic microstructure, the matrix consisted of randomly distributed dislocations with no defined cell structure contrary to that observed in the austenitic stainless steel 316L. The evolution of dislocation structure in AM processed BCC steels is only beginning to be studied as earlier studies primarily focused on tungsten, molybdenum, and other refractory metals. A recent study on PBF-LB processed duplex stainless steel showed fully ferritic structure in as-printed condition with dislocation structures similar to those observed in the present work [37].

Post-processing heat treatment is critical for AM materials to optimize their microstructure and mechanical properties particularly for demanding applications they are applied to. The microstructure of the Ni-free materials can be tunable with heat treatment. After heat treatment on Ni-free specimen, there was partial recovery, recrystallization,

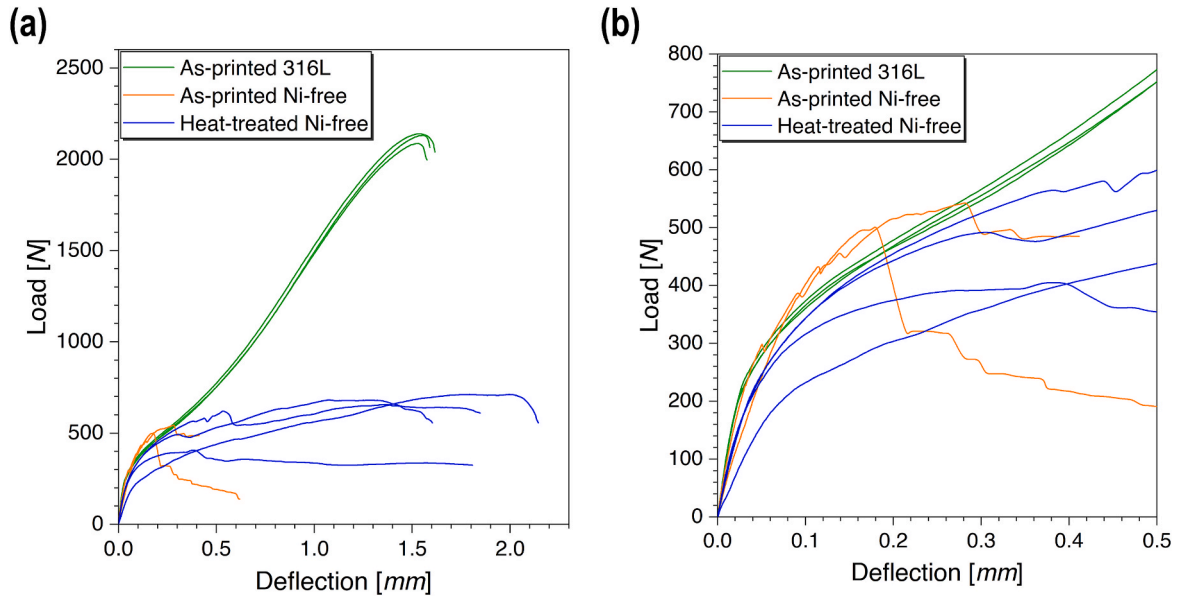

Fig. 6. Small punch testing results for PBF-LB 316L, as-printed Ni-free stainless steel, and heat-treated Ni-free stainless steel samples. (a) Full range of load–displacement curves, (b) Expanded view of the initial load–displacement region to highlight early-stage mechanical response.

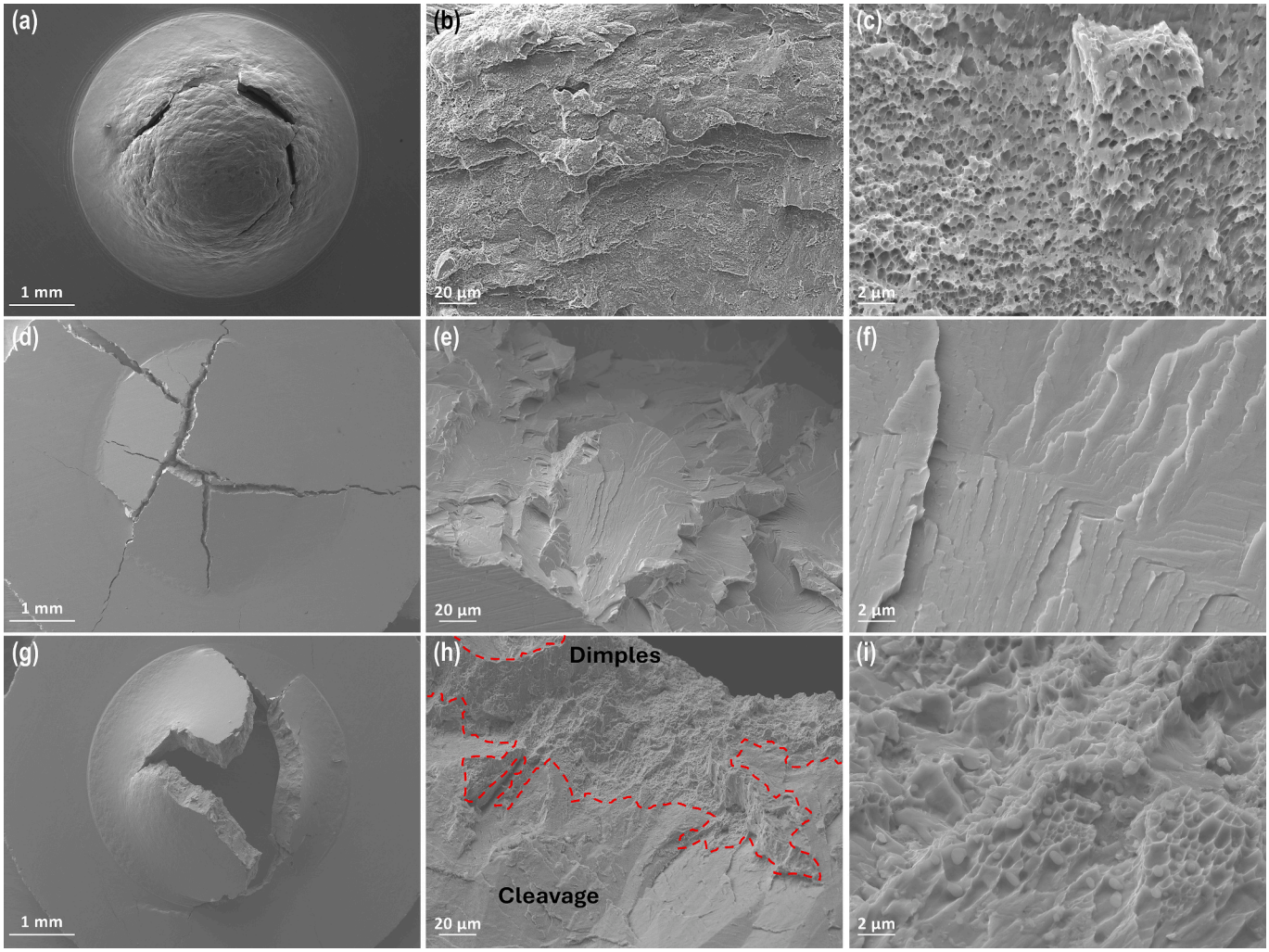

Fig. 7. SEM images of the fracture surfaces on small punch tested PBF-LB (a-c) 316L, (d-f) as-printed Ni-free stainless steel and (g-i) heat-treated Ni-free stainless steel samples.

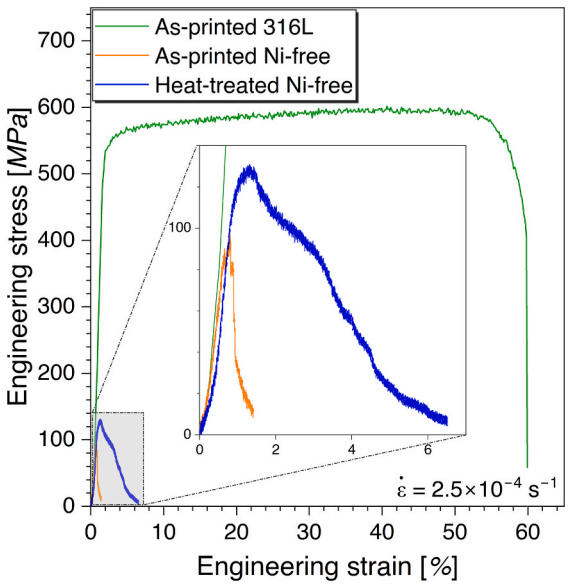

Fig. 8. Stress-Strain curves of PBF-LB 316L, as-printed Ni-free stainless steel, and heat-treated Ni-free stainless steel samples at the strain rate of 2.5 × 10^{-4} s^{-1} and room temperature.

grain growth, and phase transformation leading to the formation of austenite and secondary Chi phase with coarser ferritic grains. Such diffusion-based transformation of ferrite to austenite upon isothermal heat treatment after PBF-LB processing has also been recently reported in duplex stainless steel [37]. The EDS results presented in Fig. 2(k-o) clearly indicate higher Mo concentration in Chi phase compared to the surrounding matrix, which is consistent with the known elemental partitioning behavior of Mo [38]. Among the matrix phases, the enrichment of Mn in the FCC phase and the relatively higher concentrations of Cr and Mo in the BCC phase align with the established phase-stabilizing effects of these elements [39]. Moreover, stacking faults were observed in the newly formed FCC grains, while remnant dislocations were present in the BCC grains, as shown in Fig. 3. In contrast, no stacking faults were observed in the as-printed 316L stainless steel. This distinct behavior of the austenitic FCC grains in these two materials can be attributed to their compositional differences. A key difference is the negligible Ni content and higher Mn concentration in Ni-free stainless steel compared to 316L alloy. Both of these compositional factors contribute to a lower stacking fault energy in the Ni-free stainless steel, thereby promoting the formation of stacking faults in its FCC grains [33]. In a recent study by Nie *et al.* [40] on as-printed PBF-LB processed duplex stainless steel, stacking faults were observed in austenite and irregularly distributed dislocation structures were present in the ferrite. Under cyclic thermal stresses, as those experienced during PBF-LB processing due to repeated heating and cooling of printed layers, strain accommodation mechanisms differ markedly between ferrite and austenite. In ferrite, dislocations proliferate via mechanisms like cross-slip, forming irregular, networked distributions that help alleviate local stress. In contrast, austenite accommodates strain through the formation of intrinsic and extrinsic stacking faults due to disruptions in its FCC stacking sequence.

4.2. *Microstructure – Mechanical property relationship in PBF-LB parts*

Small punch testing, nanoindentation, miniaturized tensile testing, and post-test characterizations revealed the influence of distinct printing-induced microstructural features — such as phases, dislocation configurations, and grain structures — on the resultant significant variations in mechanical properties of the studied materials. The resultant nanohardness and microhardness of the investigated materials was an interplay of several factors such as relative fraction of austenite and ferrite, precipitates, grain size and boundaries as well as the GNDs, which are discussed in detail below.

In the present work, the ferrite phase in as-printed Ni-free steel is harder than the austenite phase in 316L, which is consistent with the analysis conducted by Gadelrab *et al.* [41] and Siegmund *et al.* [42] for the mechanical behavior of these two phases at room temperature. The heat-treated Ni-free steel contains both ferrite and austenite phases, therefore, its hardness falls between the as-printed Ni-free steel and 316L. Previous studies have shown that carbon content in ferritic-austenitic duplex steels can have significant impact on the relative hardness of austenite compared to ferrite. For a dual phase steel with similar carbon content as the Ni-free steel used in this study, it has been found through nano- and micro-indentation hardness measurements that austenite exhibited higher hardness than the ferrite [43], which was explained by the higher work hardening rate of austenite compared to ferrite [44]. However, in another study on nanoindentation of such dual phase steel, the ferrite was found to be harder than the austenite [45]. The reported contradictory observations in literature can be attributed to several microstructural features in addition to the relative fraction of austenite and ferrite. Previous studies have also shown that mechanical behavior of even the same phase in different steels can exhibit variation owing to differences in material history, *i.e.*, heat treatment, and internal stresses, *etc.* [46]. In the present study, austenite formation upon heat

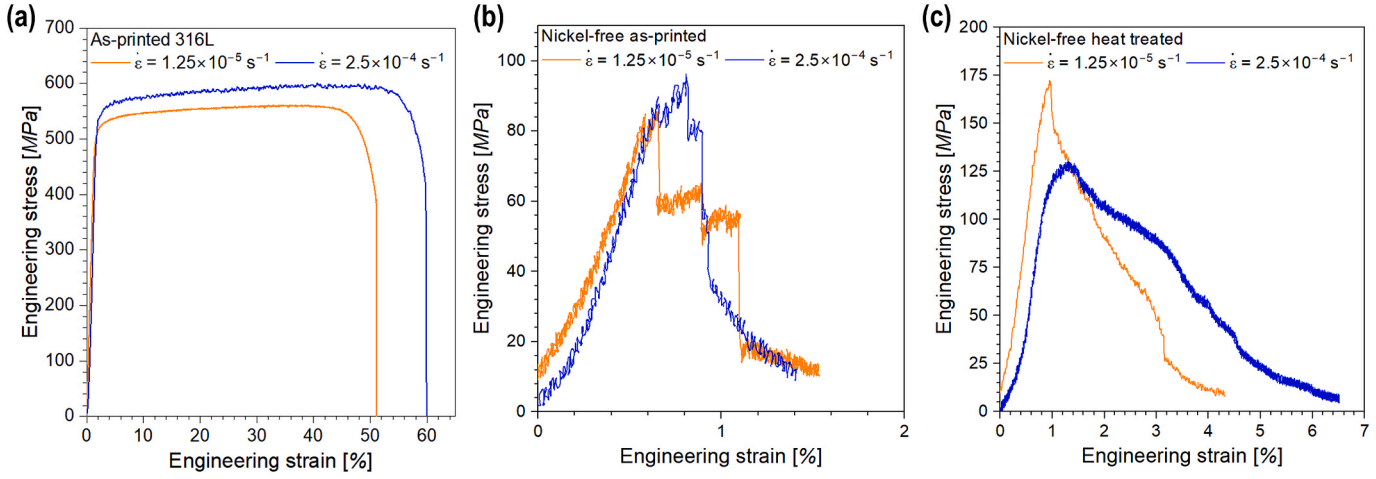

Fig. 9. Stress-Strain curve of PBF-LB (a) 316L, (b) as-printed Ni-free stainless steel and (c) heat-treated Ni-free stainless steel samples at strain rates of 1.25 × 10^{-5} s^{-1} and 2.5 × 10^{-4} s^{-1}.

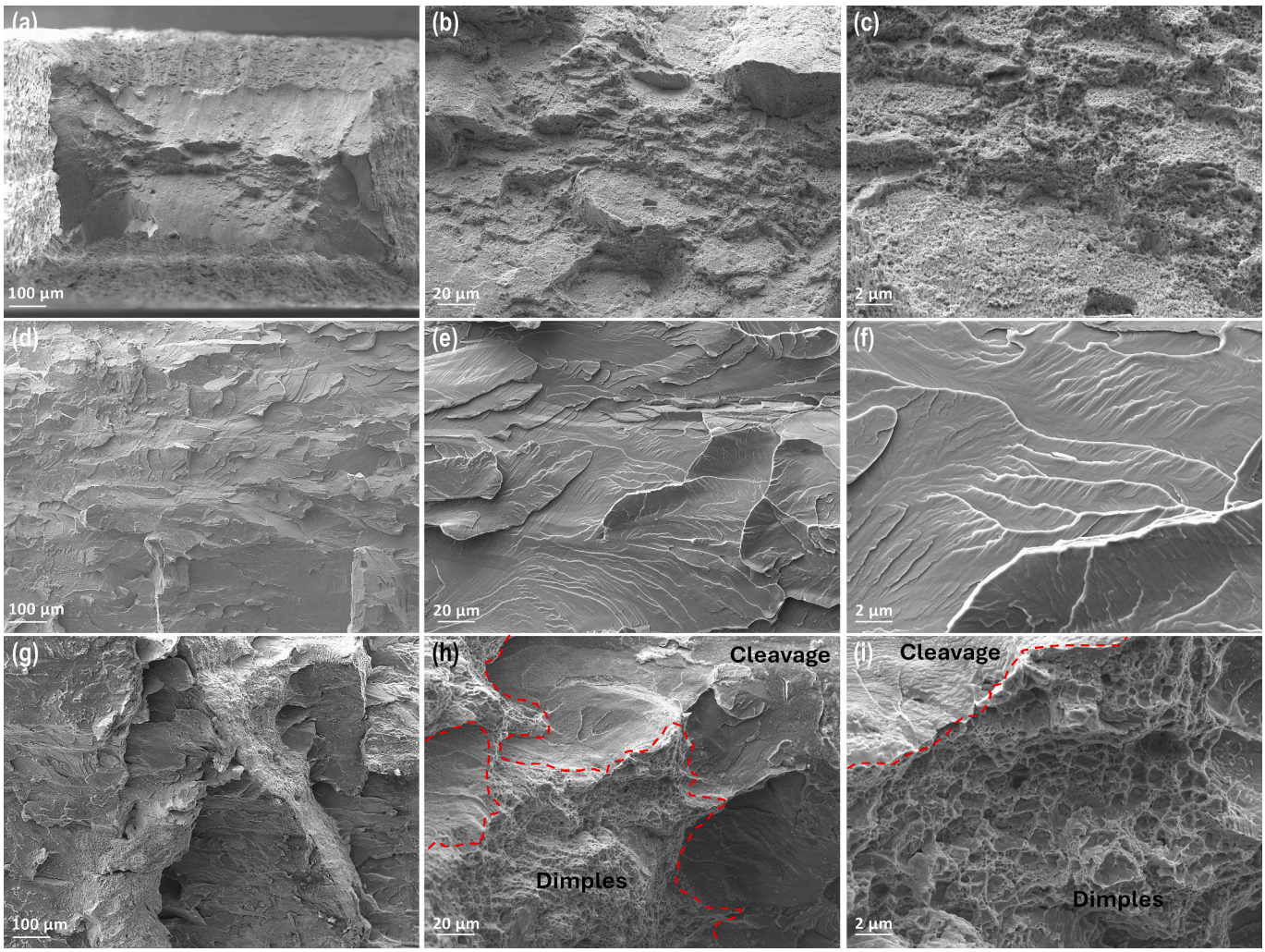

Fig. 10. SEM images of the fracture surface PBF-LB (a-c) 316L, (d-f) as-printed Ni-free stainless steel and (g-i) heat-treated Ni-free stainless steel samples tested at the strain rate of 2.5×10^{-4} s^{-1} and room temperature.

treatment was accompanied by reduced hardness. The presence of Chi phase can influence hardness through competing mechanisms. Chi phase can impede dislocation motion during plastic deformation, thereby contributing to strengthening, but its formation consumes Mo, which reduces solid-solution strengthening in the matrix and may lead to softening effect [47].

The heat-treated Ni-free stainless steel sample also exhibited a higher fraction of HAGBs compared to the as-printed condition—typically a feature associated with increased strength—this did not translate to higher hardness. In PBF-LB processed as-printed 316L, Chen *et al.* [48] have found dislocation strengthening to have the largest contribution to strengthening and significantly more than grain boundary strengthening. The present observations are consistent with these earlier findings. Furthermore, while the as-printed Ni-free steel exhibited a high density of random dislocations within the BCC matrix, the subsequent heat treatment led to partial recovery and annihilation of these dislocations, reducing internal lattice strain and thus decreasing hardness in the BCC phase. KAM and ECCI analysis demonstrate that dislocation density decreases upon heat treatment. The stacking fault density in the FCC phase and associated strain hardening were not sufficient to compensate for the loss of dislocation hardening in the BCC phase.

The 316L specimens exhibited higher tensile strength than the Ni-free stainless steel specimens. In PBF-LB processed 316L, the cell walls which are tangled with dislocations provide a unique strengthening mechanism by effectively impeding dislocation motion. This structure contributes to the simultaneous enhancement of both yield strength and ductility as reported in several studies [49–51]. The nano-sized oxides can also provide additional dispersion strengthening effect to PBF-LB 316L material. The relatively higher tensile strength and ductility in heat treatment material compared to the as-printed Ni-free steel can be attributed to the strengthening provided by grain refinement due to the presence of two phases [39]. A number of studies have attempted to correlate small punch testing results with conventional tensile properties in steels [52,53], demonstrating that maximum punch load and fracture displacement can serve as reliable indicators of ultimate tensile strength and ductility, respectively. Li *et al.* [52] performed small punch tests on three different high-strength stainless steels and found that the yield stresses estimated from small punch tests were within ±50 % of the corresponding tensile test values. Jeffs *et al.* [53] attempted to correlate tensile properties of laser powder bed fused duplex stainless steel 2205 using the small punch test across a range of temperatures up to 750 °C. The uniaxial high-temperature mechanical properties of PBF-LB duplex stainless steel 2205 in both as-built and heat-treated conditions showed trends consistent with those reported in the literature for conventionally manufactured duplex stainless steel 2205. In the present study, the uniaxial tensile strengths of as-printed PBF-LB 316L are consistent with small punch testing results, confirming that the observed high strength and ductility are associated with the characteristic dislocation cell structures and nano-oxide dispersion. These correlations reinforce that the strengthening mechanisms identified from conventional tensile

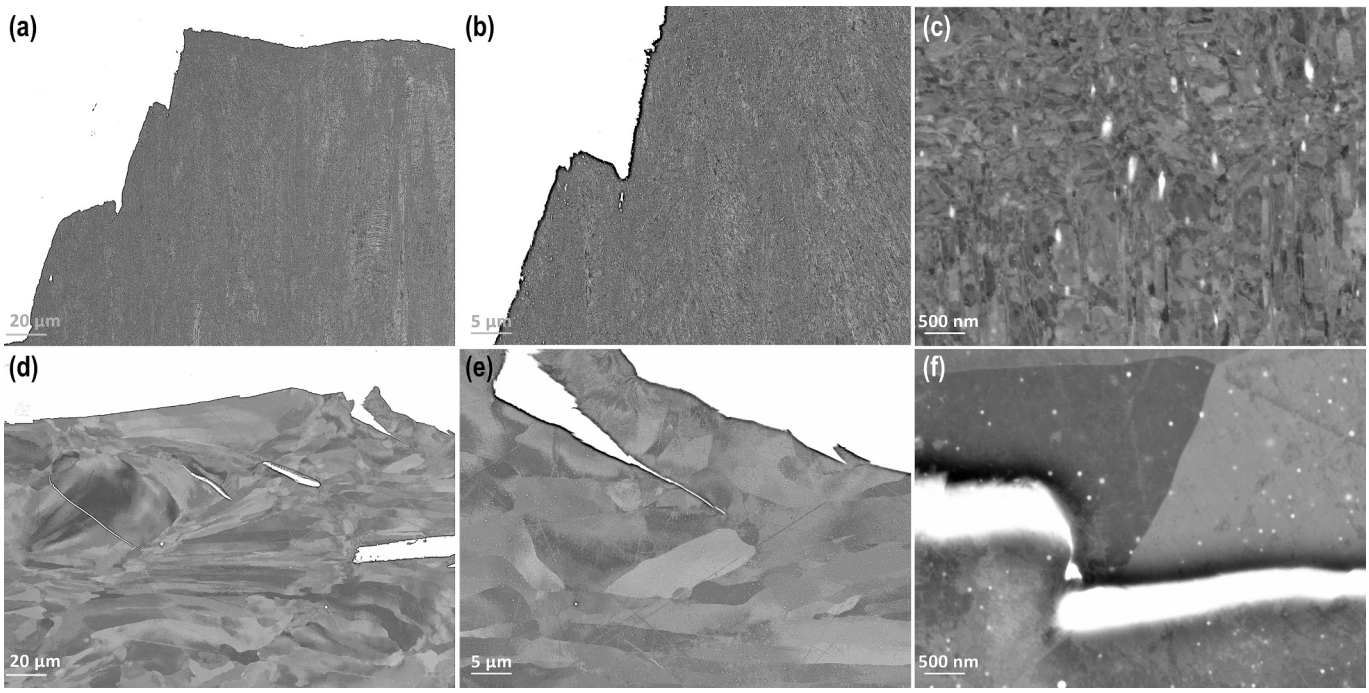

Fig. 11. Cross-sectional BSE images of the PBF-LB (a-c) 316L and (d-f) as-printed Ni-free stainless steel tested at a strain rate of 2.5×10^{-4} s^{-1}; the loading direction was vertical.

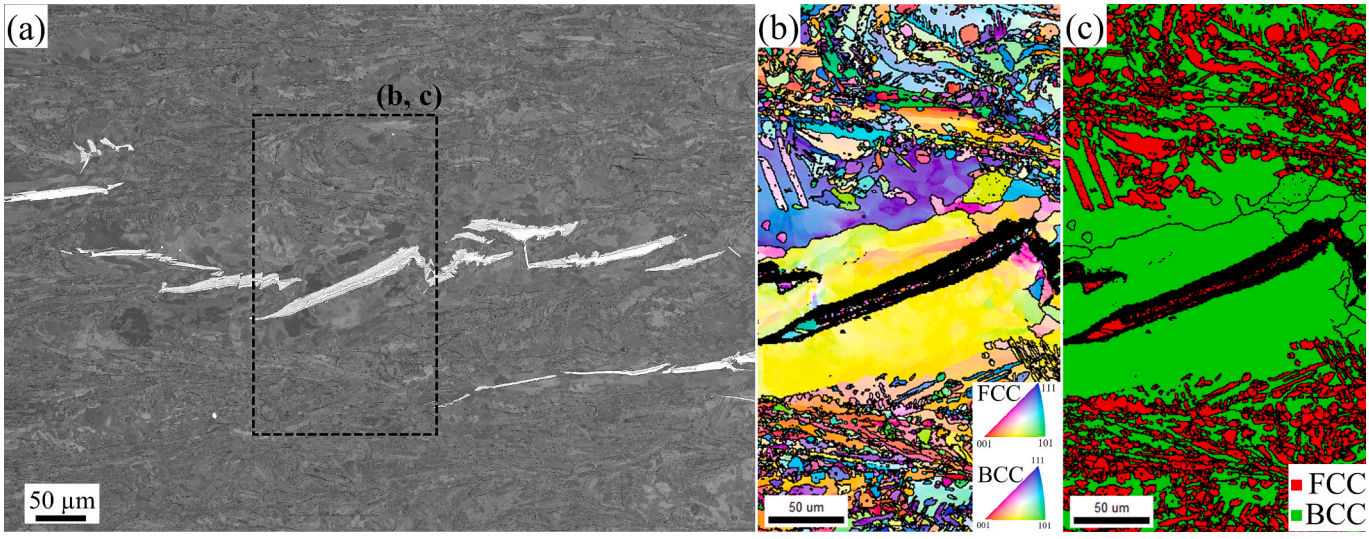

Fig. 12. Cross-sectional (a) BSE image and EBSD (b) IPF and (c) phase maps (the two major phases indexed, from the region highlighted in (a) of the heat-treated Ni-free stainless steel sample tested at a strain rate of 2.5×10^{-4} s^{-1}; the loading direction was vertical.

testing are similarly reflected under small punch testing conditions, demonstrating the reliability of small punch testing for evaluating PBF-LB 316L, particularly when only limited material is available.

To gain a more comprehensive understanding of mechanical behavior under different loading conditions, the strain rate sensitivity of the materials was also investigated. The increase in yield stress at higher strain rates observed in both 316L stainless steel and as-printed Ni-free steel can be primarily attributed to the limited time available for dislocation motion and energy dissipation at higher strain rates. This constraint enhances the resistance of material to plastic deformation, thereby resulting in higher strength. Heat treatment of Ni-free steel led to a bimodal microstructure, decrease in dislocation density, and formation of stacking faults and twin boundaries, which resulted in an increase in yield stress at the lower strain rate. Although the heat-treated Ni-free steel exhibits ≈92 % HAGBs, which are typically associated with enhanced strain rate sensitivity, competing mechanisms such as Chi-phase-assisted crack initiation, reduced dislocation density after recovery, and twin/stacking-fault-dominated slip appear to dominate, leading to an overall negative strain rate sensitivity. The observed negative strain rate sensitivity has been previously observed in dual phase steel [54]. Overall, this suggests that both strain-rate-dependent and microstructure-dependent mechanisms contribute to the hardening behavior of the Ni-free steel under different testing conditions [55].

4.3. *Microstructure – failure mechanism correlation in PBF-LB parts*

Failure or fracture is a process governed by the synergistic interaction between the material's baseline microstructure and the deformation

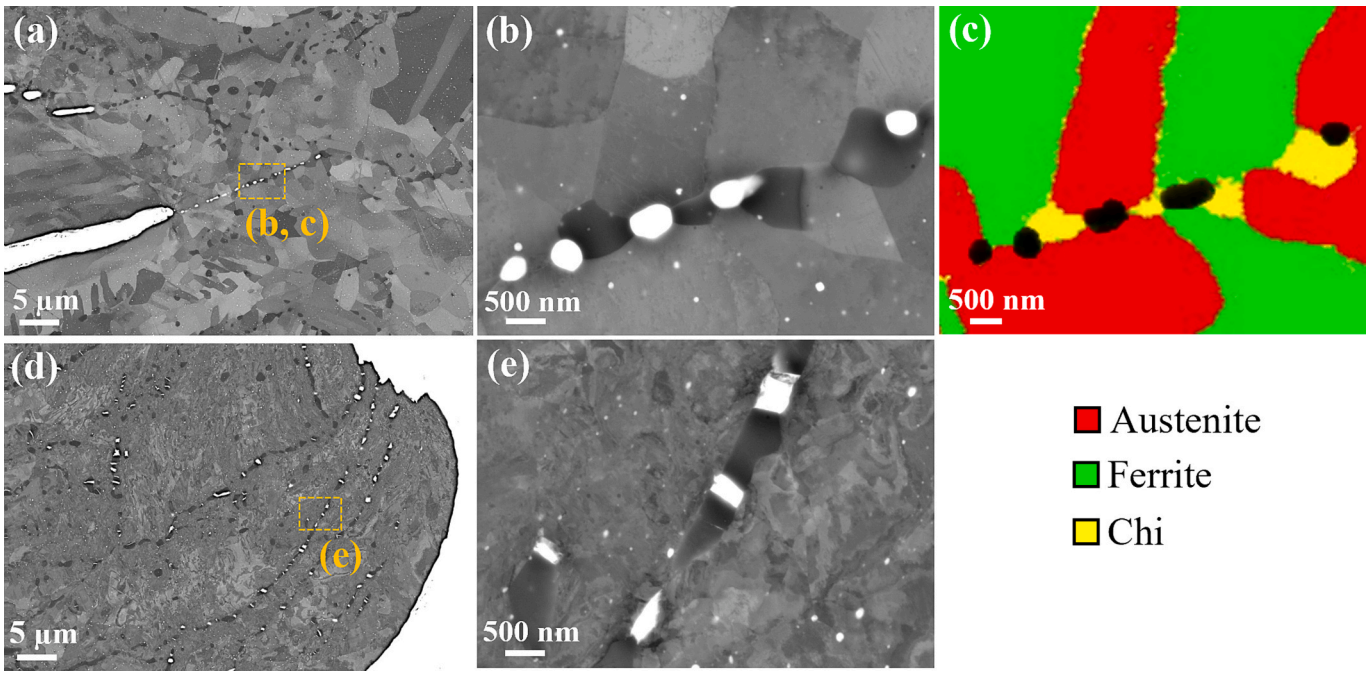

Fig. 13. Cross-sectional BSE images of the PBF-LB heat-treated Ni-free stainless steel samples at a strain rate of 2.5×10^{-4} s^{-1}. (a-b) location 1 under the cleavage fracture surface and (d-e) location 2 under the ductile fracture surface; EBSD phase map corresponding to (b) is also provided in (c). The voids/crack appear white in BSE images and black in the EBSD map.

induced by loading. Deformation behavior is not solely governed by the static microstructure but is also strongly influenced by the dynamic loading and stress conditions specific to each testing method [56,57]. Small punch tests and miniaturized tensile tests are different in their loading methods. This discrepancy is attributed to the more constrained deformation zone and the elevated triaxial stress state inherent to the small punch test, which promotes earlier damage initiation and reduces the ability of material to accommodate plastic flow.

The evident necking and extensive plastic deformation were attributed to the nanovoid and microvoid formation in 316L material. As-printed ferritic Ni-free stainless steel specimen exhibited transgranular cleavage fracture with minimal deformation, while the heat-treated specimen displayed a mixed fracture mode combining cleavage and ductile features. This brittle fracture behavior in the as-printed condition can be attributed to the inherent tendency of fully ferritic steels to exhibit mechanical brittleness close at room temperature [58]. In contrast, the change in fracture mode following heat treatment is primarily due to the formation of a duplex microstructure containing both ferrite and austenite phases. As shown in Fig. 10(g-i), a mixed mode of fracture was revealed in heat-treated Ni-free stainless steel, where ductile tearing ridges with dimples can be observed between the cleavage parts with transgranular brittle fracture. Similar mixed deformation behaviors have been reported in thermally aged cast duplex steels, where brittle cleavage occurred in ferrite and ductile shearing in austenite [59].

Although the heat-treated Ni-free stainless steel exhibited certain features of ductile fracture, the overall ductility remained limited, with preferential crack propagation in the coarse ferritic grains. In duplex stainless steel tested in ambient conditions as in the present study, Laukkanen *et al.* [60] reported the detrimental influence of coarse ferritic grains on cleavage initiation. The low ductility in the heat treated Ni-free material could also be due to the additional embrittling effect of Chi phase precipitates. The Chi phase facilitated crack initiation and propagation, particularly through the formation of nanometer-sized voids at the Chi/matrix interface, contributing to premature failure. In duplex stainless steel subjected to environmentally assisted cracking, Azevedo *et al.* [61] observed preferential crack propagation through the ferritic phase and along austenite/ferrite interfaces, a mechanism further intensified by the presence of undesirable intermetallic phase precipitates. This cracking behavior is in line with observations in the present study with testing in ambient conditions. Moreover, interfaces between coarse- and fine-grained regions are known to exhibit pronounced strain localization, which may have also contributed to the cracking observed in the heat-treated Ni-free material with a bimodal grain structure.

To enhance the industrial applicability of PBF-LB Ni-free stainless steels and mitigate the risk of premature failure, several key strategies should be considered. The nitrogen content in the powder can be further increased and its consequent role on mechanical behavior of the material should be assessed. For instance, nitrogen is known to strengthen both the austenitic and ferritic phases [39,58], however its effect on toughness of stainless steel is not well established [62]. Moreover, PBF-LB processing parameters should also be optimized to reduce the pre-existing cracks in the material. The chemical composition and heat treatment procedure for the Ni-free steel can be tuned to limit the detrimental Chi phase formation.

5. Conclusions

This work systematically investigated the microstructural evolution, mechanical behavior, and failure mechanisms of PBF-LB Ni-free and 316L stainless steels, which are governed by a complex interplay of phase composition, dislocation structures, grain boundary characteristics, and strain rate sensitivity. The following quantitative conclusions can be drawn from this research:

- The as-printed 316L exhibited a fully austenitic structure with cellular dislocation networks (≈400 nm–600 nm) and nano-oxides, achieved the highest tensile strength (≈600 MPa) and ductility (≈60 %) through dislocation and dispersion strengthening and experienced ductile fracture by microvoid coalescence. In contrast, the as-printed Ni-free stainless steel showed a fully ferritic microstructure with high random dislocation density but lacked cellular substructures, exhibited the highest nanohardness (4.94 GPa) but

low tensile strength (90 MPa) and cleavage fracture with negligible plasticity (≈2 % strain).

- Heat treatment at 950 °C for 30 min followed by water quenching induced partial recrystallization, grain coarsening, and transformed the Ni-free steel into a duplex microstructure (≈41 % austenite, ≈56 % ferrite, ≈3 % Chi phase), improving its mechanical performance but introducing complex failure mechanisms influenced by Chi precipitates and grain boundary characteristics. Heat treatment led to moderate ductility (6 %), reduced hardness, and a shift from brittle cleavage to mixed-mode fracture behavior. Cracks preferentially propagated along coarse BCC grain regions and Chi precipitate interfaces, where voids nucleated under triaxial stress. Grain boundary statistics revealed an increase in HAGBs and annealing twins after post-heat treatment in Ni-free stainless steel, promoting plasticity but also causing strain localization.

These results highlight that optimizing phase composition and grain structure through heat treatment—alongside control of nitrogen content and Chi phase formation—offers a pathway to tailor Ni-free stainless steels for enhanced mechanical performance. To enhance the industrial viability of PBF-LB processed Ni-free stainless steels, future work should focus on optimizing alloy composition—particularly nitrogen and Mo content—and refining process and heat treatment parameters to suppress detrimental phase formation, promote balanced phase fractions, and improve fracture toughness.

CRediT authorship contribution statement

Siddharth Suman: Writing – review & editing, Methodology, Investigation, Funding acquisition, Formal analysis, Data curation, Conceptualization. **Sneha Goel:** Writing – review & editing, Investigation, Formal analysis, Data curation, Conceptualization. **Juhani Rantala:** Writing – review & editing, Investigation, Formal analysis, Conceptualization. **Asta Nurmela:** Writing – review & editing, Investigation, Formal analysis, Conceptualization. **Abhinav Anand:** Writing – review & editing, Investigation, Formal analysis. **Ashish Ganvir:** Writing – review & editing, Project administration, Investigation, Funding acquisition, Formal analysis, Conceptualization. **Ran Sui:** Writing – review & editing, Conceptualization. **Zaiqing Que:** Writing – review & editing, Writing – original draft, Supervision, Resources, Project administration, Methodology, Investigation, Funding acquisition, Formal analysis, Data curation, Conceptualization.

Declaration of competing interest

The authors declare that they have no known competing financial interests or personal relationships that could have appeared to influence the work reported in this paper.

Acknowledgements

VTT acknowledges the funding by the European Union – NextGenerationEU. University of Turku acknowledges the funding support from Tenure-Track grant to Prof. Ashish Ganvir; Research Council of Finland as well as European Council for co-funded M.ERANET 2022, GREENBAT (2022-2025) project and Research Council of Finland funded SOLACE, 360540 (2024-2028) project. The authors would like to express their gratitude for the experimental contributions of Mrs. Taru Lehtikuusi, Dr. Pedro Ferreiros, and Mrs. Johanna Lukin from VTT. The Authors also would like to acknowledge Mr. Aki Piiroinen and Prof. Antti Salminen for arranging resources in DMS laboratory. The authors gratefully acknowledge Prof. Efthymios Polatidis (University of Patras, Greece) for initiating the collaborative idea of additive manufacturing of Ni-free dual-phase steels together with Prof. Ashish Ganvir and Dr. Sneha Goel from the University of Turku and VTT, respectively.

Data availability

The data that support the findings of this study are available from the corresponding author upon reasonable request.

References

[1] M. Bojinov, L. Chang, Z. Saario, Z. Que, Corrosion of 316L stainless steel produced by laser powder bed fusion and powder metallurgy in pressurized water reactor primary coolant, *Materialia,* vol. 34, no. 102055, 2024.
[2] Z. Que, T. Riipinen, P. Ferreirós, S. Goel, K. Sipilä, T. Saario, T. Ikäläinen, A. Toivonen and A. Revuelta, Effects of surface finishes, heat treatments and printing orientations on stress corrosion cracking behavior of laser powder bed fusion 316 L stainless steel in high-temperature water, *Corros. Sci.,* vol. 233, no. 112118, 2024.
[3] H. Springer, C. Baron, A. Szczepaniak, E. Jägle, M. Wilms, A. Weisheit, D. Raabe, Efficient additive manufacturing production of oxide- and nitride-dispersion-strengthened materials through atmospheric reactions in liquid metal deposition, Mater. Des. 111 (2016) 60–69.
[4] G. Wang, H. Ouyang, C. Fan, Q. Guo, Z. Li, W. Yan, Z. Li, The origin of high-density dislocations in additively manufactured metals, Materials Research Letters 8 (8) (2020) 283–290.
[5] W. Jiang, Y. Zhao, Y. Lu, Y. Wu, D. Frazer, D. Guillen, D. Gandy and J. Wharry, "Comparison of PM-HIP to forged SA508 pressure vessel steel under high-dose neutron irradiation," *Journal of Nuclear Materials,* vol. 155018, no. 594, 2024.
[6] D. Kong, C. Dong, S. Wei, X. Ni, L. Zhang, R. Li, L. Wang, C. Man and X. Li, About metastable cellular structure in additively manufactured austenitic stainless steels, *Additive Manufactur.,* vol. 38, no. 101804, 2021.
[7] T. Ngo, A. Kashani, G. Imbalzano, K. Nguyen, D. Hui, Additive manufacturing (3D printing): a review of materials, methods, applications and challenges, Compos. B 143 (2018) 172–196.
[8] Y. Sun, A. Moroz, K. Alrbaey, Sliding wear characteristics and corrosion behaviour of selective laser melted 316L stainless steel, J. Mater. Eng. Perform. 23 (2014) 518–526.
[9] Z. Sun, X. Tan, S. Tor, Selective laser melting of stainless steel 316L with low porosity and high build rates, Mater. Des. 104 (2016) 197–204.
[10] X. Lou, M. Song, P. Emigh, M. Othon, P. Andresen, On the stress corrosion crack growth behaviour in high temperature water of 316L stainless steel made by laser powder bed fusion additive manufacturing, Corros. Sci. 128 (2017) 140–153.
[11] Z. Que, T. Riipinen, S. Goel, A. Revuelta, T. Saario, K. Sipilä and A. Toivonen, "SCC behaviour of laser powder bed fused 316L stainless steel in high-temperature water at 288 °C," *Corrosion Science,* vol. 214, no. 111022, 2023.
[12] Roadmap for Regulatory Acceptance of Advanced Manufacturing Methods in the Nuclear Energy Industry, Nuclear Energy Institute, 2019.
[13] Westinghouse Creates and Installs Industry's First 3D-Printed Fuel Debris Filter for Nuclear Power Plants, Westinghouse Electric Company, [Online]. Available: https://info.westinghousenuclear.com/news/westinghouse-creates-and-installs-industrys-first-3d-printed-fuel-debris-filter-for-nuclear-power-plants?utm_campaign=ogsocial&utm_content=1655125790&utm_medium=social&utm_source=linkedin. [Accessed Apr 2025].
[14] W. Tucho, V. Lysne, H. Austbø, A. Sjolyst-Kverneland, V. Hansen, Investigation of effects of process parameters on microstructure and hardness of SLM manufactured SS316L, J. Alloy. Compd. 740 (2018) 910–925.
[15] M. Godec, S. Zaefferer, B. Podgornik, M. Šinko, E. Tchernychova, Quantitative multiscale correlative microstructure analysis of additive manufacturing of stainless steel 316L processed by selective laser melting, Mater Charact 160 (2020).
[16] R. Belles, W. Poore, T. Harrison, M. Muhlheim, T. Muth, A Survey of Additive Manufacturing Capabilities, ORNL/TM-2018/1013, 2018.
[17] Y. Kok, X. Tan, P. Wang, M. Nai, N. Loh, E. Liu, S. Tor, Anisotropy and heterogeneity of microstructure and mechanical properties in metal additive manufacturing: a critical review, Mater. Des. 139 (2018) 565–586.
[18] J. Reijonen, R. Björkstrand, T. Riipinen, Z. Que, S. Metsä-Kortelainen and M. Salmi, Cross-testing laser powder bed fusion production machines and powders: Variability in mechanical properties of heat-treated 316L stainless steel, *Mater. Des.,* vol. 204, no. 109684, 2021.
[19] Z. Que, L. Chang, T. Saario, M. Bojinov, Localised electrochemical processes on laser powder bed fused 316L with various heat treatments in high-temperature water, *Additive Manufacturing,* vol. 60, no. 103205, 2022.
[20] M. Audrain, Overview of US Regulatory Activities in Advanced Manufacturing, U. S. Nuclear Regulatory Commission, [Online]. Available: https://energiforsk.se/media/28428/regulatory_activities_usnrc_audrain.pdf. [Accessed April 2025].
[21] Effects of nickel on irradiation embrittlement of light water reactor pressure vessel steels, IAEA-TECDOC-1441, International Atomic Energy Agency, Vienna, Austria, 2005.
[22] B. Voronenko, Austenitic-ferritic stainless steels: a state-of-the-art review, Met. Sci. Heat Treat. 39 (1997) 428–437.
[23] G. Mudd, Global trends and environmental issues in nickel mining: Sulfides versus laterites, Ore Geol. Rev. 38 (1–2) (2010) 9–26.
[24] J. Hostynek, H. Maibach, S. Nedorost, Nickel and The Skin: Absorption, Immunology, Epidemiology, and Clinical Aspects, CRC Press, 2003.
[25] L. Patnaik, S. Maity, S. Kumar, Status of nickel free stainless steel in biomedical field: A review of last 10 years and what else can be done, *Mater. Today Proc.,* vol. 26, no. 638–643, 2020.
[26] K. Yang, Y. Ren, Nickel-free austenitic stainless steels for medical applications, *Sci. Technol. Adv. Mater.,* vol. 11, no. 014105, 2010.

[27] M. Speidel, Nitrogen containing austenitic stainless steels, Materwiss. Werksttech. 37 (10) (2006) 875–880.
[28] R. Espy, Weldability of nitrogen-strengthened stainless steels, *Welding research supplement,* pp. 149-156, 1982.
[29] S. Goel, M. Bojinov, J. Capek, T. Saario, E. Polatidis, T. Kantonen, A. Salminen, M. Blankenburg, A. Ganvir and Z. Que, Corrosion behavior of laser powder bed fusion manufactured nickel-free stainless steels in high-temperature water, *Corros. Sci.,* 239, 112410, 2024.
[30] A. Arabi-Hashemi, X. Maeder, R. Figi, C. Schreiner, S. Griffiths and C. Leinenbach, 3D magnetic patterning in additive manufacturing via site-specific in-situ alloy modification, *Appl. Mater. Today,* vol. 18, no. 100512, 2020.
[31] B. Cheng, F. Wei, W. Teh, J. Lee, T. Meng, K. Lau, L. Chew, Z. Zhang, K. Cheong, C. Ng, P. Wang, C. Tan and U. Ramanurty, Ambient pressure fabrication of Ni-free high nitrogen austenitic stainless steel using laser powder bed fusion method, *Additive Manuf.,* vol. 55, no. 102810, 2022.
[32] A. Anand, C. Nayak, E. Mäkilä, Z. Que, H. Piili, S. Goel, A. Salminen, A. Ganvir, Tribocorrosion behavior of nickel-free duplex and 316L stainless steels fabricated by laser powder bed fusion in artificial seawater, J. Mater. Res. Technol. 38 (2025) 2197–2211.
[33] R. Schramm, R. Reed, Stacking fault energies of seven commercial austenitic stainless steels, Metall. Trans. A 6 (1975) 1345–1351.
[34] N. Haghdadi, M. Laleh, M. Moyle, S. Primig, Additive manufacturing of steels: a review of achievements and challenges, J. Mater. Sci. 56 (2021) 64–107.
[35] K. Saeidi, L. Kevetkova, F. Lofaj, Z. Shen, Novel ferritic stainless steel formed by laser melting from duplex stainless steel powder with advanced mechanical properties and high ductility, Mater. Sci. Eng. A 665 (2016) 59–65.
[36] S. David, J. Vitek, R. Reed, T. Hebble, Effect of rapid solidification on stainless steel weld metal microstructures and its implications on the Schaeffler diagram, 1 September 1987. [Online]. Available: https://digital.library.unt.edu/ark:/67531/metadc1103880/. [Accessed 27 May 2025].
[37] X. He, V. Rielli, Q. Liu, X. Li, V. Luzin, Haghdadi, N. and S. Primig, "Effects of laser powder bed fusion parameters on the delta-ferrite to austenite phase transformation in duplex stainless steels," *Additive Manufacturing,* vol. 107, no. 104825, 2025.
[38] S. Jeon, H. Kim, Y. Park, Effects of inclusions on the precipitation of chi phases and intergranular corrosion resistance of hyper duplex stainless steel, Corros. Sci. 87 (2014) 1–5.
[39] R. Gunn, Duplex Stainless Steels, Microstructure, Properties and Applications, Woodhead Publishing, 1997.
[40] Y. Nie, F. Yang, L. Meng, Y. Wang, L. Yin, Q. Shi, J. Ma, W. Liang and L. Zheng, Materials Science and Engineering: A, *Dislocation structures and residual stresses in duplex stainless steel fabricated by laser powder bed fusion with 430 and 316L powders,* vol. 914, no. 147127, 2024.
[41] K. Gadelrab, G. Li, M. Chiesa, T. Souier, Local characterization of austenite and ferrite phases in duplex stainless steel using MFM and nanoindentation, J. Mater. Res. 27 (2012) 1573–1579.
[42] T. Siegmund, E. Werner and F. Fischer, On the thermomechanical deformation behavior of duplex-type materials, *J. Mech. Phys. Solids,* 43, 4, 495-501, 503-532, 1995.
[43] H. Li, Z. Jiang, Z. Zhang, Y. Yang, Effect of grain size on mechanical properties of nickel-free high nitrogen austenitic stainless steel, J. Iron Steel Res. Int. 16 (2009) 58–61.
[44] A. Olanipekun, M. Nthabiseng, O. Ayodele, M. Mphahlele, B. Mampuya, P. Olubambi, Datasets on the measurement of mechanical properties of ferrite and austenite constitutive phases using nanoindentation and micro hardness techniques, *Data Br.,* vol. 27, no. 104551, 2019.
[45] J. Mola, E. Seo, L. Cho, Correlation between mechanical stability and hardness of austenite in martensite/austenite mixtures, *Mater. Sci. Eng. A,* vol. 822, no. 141687, 2021.
[46] A. Al Motasem, M. Posselt, J. Bergström, Nanoindentation and nanoscratching of a ferrite/austenite iron bi-crystal: an atomistic study, Tribol. Int. 127 (2018) 231–239.
[47] H. Lu, H. Guo, W. Liang, X. Shen, The precipitation behavior and its effect on mechanical properties of cold-rolled super-ferritic stainless steels during high-temperature annealing, J. Mater. Res. Technol. 12 (2021) 1171–1183.
[48] S. Chen, G. Ma, G. Wu, A. Godfrey, T. Huang, X. Huang, Strengthening mechanisms in selective laser melted 316L stainless steel, *Mater. Sci. Eng. A,* vol. 832, no. 142434, 2022.
[49] Y. Wang, T. Voisin, J. McKeown, J. Ye, N. Calta, Z. Li, Additively manufactured hierarchical stainless steels with high strength and ductility, Nat. Mater. 17 (2017).
[50] J. Li, M. Yi, H. Wu, Q. Fang, Y. Liu, B. Liu, K. Zhou, P. Liaw, "Fine-grain-embedded dislocation-cell structures for high strength and ductility in additively manufactured steels," *Materials Science and Engineering: A,* vol. 790, no. 139736, 2020.
[51] S. Guo, J. Xu, J. Gu, Y. Peng, Q. Zhou, K. Wang, Effect of cellular structure on the mechanical properties of 316L stainless steel fabricated by EBF3, J. Mater. Res. Technol. 25 (2023) 5469–5482.
[52] R. Li, W. Wei, R. Chen, M. Wu, Y. Lai, Evaluating the tensile properties of high-strength stainless steels using small punch testing, *Sci. Progr.,* vol. 107, no. 3, 2024.
[53] S. Jeffs, R. Douglas, W. Beard, M. Coleman, J. Adams, T. Jones, D. Poole and R. Lancaster, Characterising the high temperature tensile behaviour of laser powder bed fused duplex stainless steel 2205 using the small punch test, *Mater.als Characterizat.,* vol. 189, no. 111953, 2022.
[54] C. Huang, M. Wang, K. Zhu, A. Perlade, M. Huang, Carbon-induced negative strain-rate sensitivity in a quenching and partitioning steel, *Acta Mater.,* vol. 255, no. 119099, 2023.
[55] D. Liu, D. Yang, Y. Hou, Y. Li, G. Wang, H. Yi, Strain rate effects on mechanical properties, microstructural evolution, and deformation mechanisms of high manganese steels, J. Mater. Sci. Technol. 237 (2025) 219–255.
[56] Y. Ge, L. Chang, M. Bojinov, T. Saario, Z. Que, Mechanistic understanding of the localized corrosion behavior of laser powder bed fused 316L stainless steel in pressurized water reactor primary water, *Scripta Materialia,* vol. 238, no. 115764, 2024.
[57] M. Bojinov, T. Saario, Y. Ge, L. Chang and Z. Que, "Effect of hydrogen on electrochemical behavior of additively manufactured 316L in pressurized water reactor primary water," *Corrosion Science,* vol. 224, no. 111557, 2023.
[58] L. Jacquet, N. Meyer, M. Libert, F. Geuser, M. Braccini, R. Estevez, M. Mantel, Study of cleavage fracture in ferritic stainless steels part I: Development and characterization of model microstructures, *Mater. Sci. Eng.: A,* vol. 864, no. 144534, 2023.
[59] S. Li, Y. Wang and X. Wang, In situ observation of the deformation and fracture behaviors of long-term thermally aged cast duplex stainless steels, *Metals,* vol. 9(2), no. 258, 2019.
[60] A. Laukkanen, S. Uusikallio, M. Lindroos, T. Andersson, J. Kömi and D. Porter, Micromechanics driven design of ferritic–austenitic duplex stainless steel microstructures for improved cleavage fracture toughness, *Eng. Fracture Mech.,* 253, no. 107878, 2021.
[61] C. Azevedo, H. Pereira, S. Wolynec, A. Padilha, An overview of the recurrent failures of duplex stainless steels, Eng. Fail. Anal. 97 (2019) 161–188.
[62] I. Woo, Y. Kikuchi, Weldability of high nitrogen stainless steel, ISIJ Int. 42 (12) (2002) 1334–1343.